**EPJ manuscript No.**
(will be inserted by the editor)

# 3D solutions of the Poisson-Vlasov equations for a charged plasma and particle core model in a line of FODO cells

G. Turchetti[1], S. Rambaldi[1], A. Bazzani[1], M. Comunian[2], and A. Pisent[2]

[1] Dipartimento di Fisica and INFN, Via Irnerio 46, 40126 Bologna ITALY
[2] INFN Laboratori Nazionali di Legnaro, ITALY

the date of receipt and acceptance should be inserted later

**Abstract.** We consider a charged plasma of positive ions in a periodic focusing channel of quadrupolar magnets in presence of RF cavities. The ions are bunched into charged triaxial ellipsoids and their description requires the solution of a fully 3D Poisson-Vlasov equation. We also analyze the trajectories of test particles in the exterior of the ion bunches in order to estimate their diffusion rate. This rate is relevant for a high intensity linac (TRASCO project). A numerical PIC scheme to integrate the Poisson-Vlasov equations in a periodic focusing system in 2D and 3D space dimensions, is presented. The scheme consists in a single particle symplectic integrator and a Posisson solver based on FFT plus tri-diagonal matrix inversion. In the 2D version arbitrary boundary conditions can be chosen. Since no analytical self consistent 3D solution is known, we chose an initial Neuffer-KV distribution in phase space, whose electric field is close to the one generated by a uniformly filled ellipsoid. For a matched (periodic) beam the orbits of test particles moving in the field of an ellipsoidal bunch, whose semiaxis satisfy the envelope equations, is similar to the orbits generated by the self consistent charge distribition obtained from the PIC simulation, even though it relaxes to a Fermi-Dirac like distribution. After a transient the rms radii and emittances have small amplitude oscillations. The PIC simulations for a mismatched (quasiperiodic) beam are no longer comparable with the ellipsoidal bunch model even though the qualitative behaviour is the same, namely a stronger diffusion due to the increase of resonances.

**PACS.** 29.20.Hm – 29.27.Ac – 52.40.Mj – 11.10.Ef

## 1 Introduction

High intensity linacs are being considered for a variety of applications such as nuclear wastes transmutation, neutron spallation sources and inertial fusion. One of the major problems is the control of the beam quality, namely of the losses from the core. The core is formed by positive ions moving in a quadrupolar magnetic field, which focuses them transversally and in radio frequency cavities (RF) which focus them longitudinally. The standard approach is based on the Poisson-Vlasov equations because the plasma has a very low collisionality. If the longitudinal focusing is absent, as it is the case of circular machines after the acceleration stage, the problem becomes 2D and the analytic Kapchinsky-Vladimirsky (K.V.) [1, 2] solutions are known also if the transverse focusing is periodic. If the transverse and longidudinal focusing are both constant, then the Hamiltonian is a first integral and a self consistent distribution can be written. We analyze the physical case for a linac with a periodic transverse and logitudinal focusing, where no analytic solution is known. The key issues are equilibrium distributions of ions and the diffusion of test particles due to resonances with the ions collective oscillations, which may explain the formation of a halo around the ions core. For a constant focusing model and azimuthally symmetric K.V. beam, the $1/2$ resonance between the transverse oscillations of a particle due to quadrupolar fields (betatron oscillations) and the (mismatch) oscillations of the core was proposed as the mechanism for the halo formation [3]. Small perturbations from a uniform charge density in the core were shown to provide a possible escape mechanism [4,5]. The same model was explored numerically for smooth self consistent nonstationary distributions [6]. The dynamics of a test particle has been investigated also in the periodic focusing case and the key role of the mismatch oscillations in the diffusion process leading the halo formation was confirmed [7,8]. Such a result was obtained using the Frequency Map Analysis (FMA) on the particle-core model (PC) for a KV beam; the presence of an additional frequency prevents the use of the Poincaré map first proposed to study the constant focusing models [9]. The analysis has shown that the test particles are better confined if the horizontal and vertical tunes are not equal, since in this case the strong resonance $\nu_x = \nu_y$ is avoided. The result was confirmed by the numerical solution of the Poisson-Vlasov equations using FFT and symplectic integration [10,11], which corresponds to the particle in cell method

(PIC) used in plasma physics [12] and beam dynamics [13]. The proposed Poisson solver allows to impose Dirichelet conditions on an arbitrary boundary, doubling the computational complexity.

In a linac the dynamics is essentially 3D since the frequencies are comparable and the rms dimensions of a bunch of ions are of the same order of magnitude. As a consequence a three dimensional model for the halo formation has to be considered. Recently a 3D constant focusing model has been proposed for azimuthally symmetric bunches corresponding to a self consistent phase space distribution, function of the Hamiltonian [14]. In this case the PIC simulations show that longitudinal and transverse halos develop when the beam is mismatched and the mismatch frequencies agree with the analytical PC estimates for small elongation of the bunch. The periodic focusing model is certainly more appropriate for a realistic linac but no self consistent solution of the Poisson Vlasov equations is known and no azimuthal symmetry can be assumed.

We have developed a fully 3D PIC code to solve the Poisson-Vlasov equations: the particles evolution is based on a symplectic integrator, the Poisson solver on FFT. The initial distribution is the product of a KV in transverse phase space times a Neuffer[15] distribution in longitudinal phase space. The configuration space projection of our distribution is a cylinder with uniform transverse density and parabolic longitudinal density. This distribution has been chosen because its projections on the tranverse and longitudinal phase spaces are self consistent solutions of the 2D and 1D Poisson Vlasov equations. The overall distribution is not stationary but the numerical simulations show that the rms radii have modest variations. We have compared the cylindrical KV-Neuffer distribution with a uniform distribution on an ellipsoid having the same rms radii. On the slices obtained by cutting the cylinder and the ellipsoid with the same transverse planes $z$ and $z+dz$, the charge is the same and the cylinder density is proportional to the ellipsoid cross section since the density of the latter is constant. The transverse electric field generated by the parabolic charge distribution in the cylinder is very close to the field generated by the uniformly charged ellipsoid. The longitudinal electric fields are also very close to each other around the center, and the discrepancy exhibits a moderate increase with the longitudinal distance. The chosen initial phase space distribution rapidly relaxes to a new one, fitted with a Fermi-Dirac distribution, since it devoleps a Maxwellian queue but remains almost uniform close to the center. Nevertheless the electric field has a modest variations. The rms emittances have initially some low frequency oscillations while there is a relaxation to a new equilibrium. We have systematically performed a benchmarking of the 2D version of the code with the analytical KV solution. The observed steady emittance growth is explained as a numerical noise effect [10,20], the sudden rises, observed for unequal linear frequencies, as an effect of the numerical mismatch, which can excite linearly unstable modes. In these cases a nonlinear stability analysis would be needed to understand the observed asysmptotic behaviour of the beam parameters, by extending the results obtained in the constant focusing case [21].

The numerical study of the halo formation requires a comparison between the integration of the Poisson-Vlasov equations with the tracking results of the PC model. The Poisson Vlasov solver introduces a cutoff on the Fourier expansion of the space charge field, that could seriously affect the single particle dynamics far from the beam core since the Hamiltonian chaos, present in this region, is very sensitive to the high frequency components of the spectrum. On the contrary the PC model considers a uniform distribution for the beam core, which is not a self consistent solution of the Poisson Vlasov problem and cannot explain the spilling of particles from the core, that is an essential point to understand the halo formation [21]. The PC model is affected by important errors for the orbits of test particles inside or nearby the beam core, but can describe the diffusion of test particles due to resonance overlapping up to large amplitudes. It is crucial to understand to what extent we can rely on the results of the PC model.

We have developed a PC model for a uniform charge distribution on a triaxial ellipsoid whose semiaxis satisfy the envelope equations. The frequency map analysis (FMA) on the test particles confirms that the resonances between the betatron oscillations and the mismatch oscillations of the bunch create chaotic regions in phase space, which contribute to the halo formation [16]. Since a self consistent phase space distribution whose projection is a uniform elipsoidal bunch does not exist, in order to validate the PC model it is important to show that a self consistent distribution with approximately the same r.m.s. radii and the same electric field components can be found so that the dynamical behaviour of a test particle out of the core does not change appreciably. The chosen KV-Neuffer distribution satisfies there requirements. We have verified that the small amplitude high frequency mismatch [18,19] oscillations of the beam of the PIC solution agree with the envelope modes computed in the PC model. The comparison of the regular (non resonant or resonant) orbits for a test particle in a matched beam beyond 2 rms shows a fair agreemet for a few hundreds of periods, each period corresponding to a FODO cell. In the 2D case the comparison is excellent up to thousands of cells. In order to overcome the phase error, which affects the comparison of phase plots and linearly increases with the iteration number, we have performed a FMA of the PIC and PC test particle orbits. The results show that the location of the main resonances is about the same in both cases and the extent of the chaotic region is comparable.

A direct comparison of the orbits on the mismatched case is quite hard even for the 2D case, due to the presence of a large number of resonances and chaotic regions so that the results are very sensitive to the choice of the initial conditions. The correspondence is recovered if a global analysis of the phase space is performed.

The results of the present analysis show that the PC model is adequate to describe the main dynamical features of the 3D dynamics of a matched beam. Further inversti-

gations are needed to reach the same conclusions for the mismatched case and to understand the new self consistent equilibrium to which the PIC simulations evolve.

## 2 The model

We consider a FODO cell with a thin cavity described by the following Hamiltonian

$$H = \frac{p_x^2+p_y^2+p_z^2}{2} + k(s)\frac{x^2-y^2}{2} - k_{_C}(s)\,\frac{x^2+y^2}{4}$$

$$+k_{_C}(s)\frac{z^2}{2} + \frac{\xi}{2}V(x,y,z,s) \qquad (1)$$

where $k(s)$ and $k_{_C}(s)$ are piecewise constant functions describing the actions of transverse focusing and of the RF cavity respectively. We denote by $V$ the Coulomb potential produced by a bunch of unit charge and $\xi$ is the perveance defined by

$$\xi = \frac{2qQ}{v_0 p_0 \gamma^2} = \frac{2}{3}\left(\frac{3\,N\,q^2}{mc^2\beta^2\gamma^3}\right) \qquad (2)$$

where $Q = Nq$ is the total charge of the bunch for a proton beam, $q$ is the charge of a macro-particle and $p_0 = mv_0\beta$ is its momentum. For some authors the perveance is the last term of (2) within brackets, which differs from ours by the factor 3/2. To have dimensionless quantities we scale $s$ with $L$ and $x, y, z$ with $a$; the dimensionless perveance $\xi/L$ scales with $(a/L)^3$ and we still denote it by $\xi$. With the natural choice $L = 1$ m and $a = 1$ mm all the quantities become of order 1. The potential $V$ satisfies the Poisson equation

$$\Delta V = -4\pi\rho_{_S}(x,y,z,s) \qquad (3)$$

where $\rho_{_S}$ is space projection of the normalized phase space density $\rho$

$$\rho_{_S} = \int \rho(x,y,z,p_x,p_y,p_z,s)\,dp_x dp_y dp_z \qquad (4)$$

which satisfies the Liouville equation

$$\frac{\partial\rho}{\partial s} + [\rho,\,H] = 0 \qquad (5)$$

The solution of the above Poisson-Vlasov equations must be carried out self consistently and, unlikely the 2D case, no analytic solution is known.

**Optical functions** An analytical reference solution is missing. For comparison we have considered the particle in core (PC) model [9], defined by the periodic solutions of the envelope equations for a uniformly filled ellipsoidal bunch, see section 3. The electric field within a uniform ellipsoidal bunch is linear and we have computed the corresponding optical functions $\alpha_x, \beta_x,\ \alpha_y, \beta_y.\ \alpha_z, \beta_z$. The horizontal amplitude of the bunch and its derivative is given by

$$A_x = (\epsilon_{x0}\beta_x)^{1/2} \qquad p_{A_x} \equiv \frac{dA_x}{ds} = -\epsilon_{x0}\,\frac{\alpha_x(s)}{A_x(s)} \qquad (6)$$

and similar relations hold for the vertical and longitudinal components. We have used the matched optical functions of the PC model to define a set of normalized coordinates $X = \beta_x^{-1/2}x,\ P_x = (\alpha_x x + \beta_x p_x)\,\beta_x^{-1/2}$. These coordinates are convenient also to illustrate the results of the self consistent solution of equations (1,3) obtained with the PIC code.

**Phase space distribution** The initial value $\rho_0$, chosen to solve (1,3) with the PIC code, is the product of a K.V. times a Neuffer distribution [17]

$$\rho_0 = \frac{1}{\pi^2\epsilon_{x0}\,\epsilon_{y0}}\delta\left(1 - \frac{X^2+P_x^2}{\epsilon_{x0}} - \frac{Y^2+P_y^2}{\epsilon_{y0}}\right)\times$$
$$\times\frac{3}{2\pi\epsilon_{z0}}\left(1 - \frac{Z^2+P_z^2}{\epsilon_{z0}}\right)^{1/2} \qquad (7)$$

The configuration space projection is a distribution in a cylinder with elliptical base and axis along $z$, uniform on $x, y$ and parabolic in $z$ according to

$$\rho_{_S}(x,y,z) = \frac{1}{\pi\,A_x\,A_y}\,\vartheta\left(1 - \frac{x^2}{A_z^2} - \frac{y^2}{A_y^2}\right)\frac{3}{4A_z}\left(1 - \frac{z^2}{A_z^2}\right) \qquad (8)$$

The moments of the KV-Neuffer distribution are given by

$$\langle x^2\rangle = \frac{A_x^2}{4}, \qquad \langle y^2\rangle = \frac{A_y^2}{4}, \qquad \langle z^2\rangle = \frac{A_z^2}{5}$$

$$\langle x^2\rangle\langle p_x^2\rangle - \langle xp_x\rangle^2 = \frac{\epsilon_{x0}^2}{16}, \quad \langle y^2\rangle\langle p_y^2\rangle - \langle yp_y\rangle^2 = \frac{\epsilon_{y0}^2}{16}$$
$$\langle z^2\rangle\langle p_z^2\rangle - \langle zp_z\rangle^2 = \frac{\epsilon_{z0}^2}{25} \qquad (9)$$

These moments are evaluated after each cell and their variation measures the deviation from the initial distribution. We have examined a specific model corresponding to the first section of a high intensity linac, the ISCL project of the Legnaro laboratories of INFN. This is the first stage of a linac designed for nuclear wastes transmutation, TRASCO [22] project of INFN and ENEA. The main design parameters are given in table 1.

| | |
|---|---|
| Beam energy ($\beta = 0.314$) | 50 Mev |
| RF Frequency | 325 MHz |
| Period length ($8\beta\lambda$) | 2.13 m |
| Beam current | 30 mA |
| Acceleration gradient | 2.5 MV/m |
| Synchronous phase | $-40^o$ |

TABLE 1 Linac parameters

The FODO cell consists of 8 elements as shown in figure 1, and their parameters, lengths and gradients, are shown in table 2.

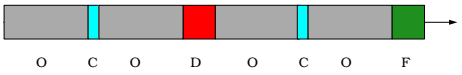


**Fig. 1.** Structure of the cell : O, C, F, D drift, RF cavity, focusing , defocusing quadrupole

The emittances of the bunch are $\epsilon_{x0} = \epsilon_{y0} = 3.02$ mm mrad and $\epsilon_{z0} = 6.81$ mm mrad. The perveance corresponding to the design current intensity is $\xi = 14.2$ but we shall consider lower values such as $\xi = 5, 10$, since the aim is to compare the PIC and PC methods and results.

| | | |
|---|---|---|
| Drift | $\ell_o = 0.5096$ m | |
| RF cavity | $\ell_c = 0.01$ m | $k_c = 44$ m$^{-2}$ |
| Focusing quad. | $\ell_{_F} = 0.05$ m | $k = 29.7$ m$^{-2}$ |
| Defocusing quad. | $\ell_{_D} = 0.05$ m | $k = 29.7$ m$^{-2}$ |

TABLE 2 Cell parameters

We denote with $A_{x0} = (\epsilon_{x0}\,\beta_{x0})^{1/2}, ...$ the bare amplitudes (zero space charge $\xi = 0$) and with $\beta_{x0}, \alpha_{x0}, ...$ the corresponding optical functions. Their values are quoted in table 3 of section 4.

## 3 The PIC code

The self consistent solution of the Poisson-Vlasov equations was obtained numerically using a PIC code. We describe here the way to generate the initial condition, the method to compute the density at the grid points and to solve the Poisson equation, the interpolation for the electric field and the symplectic integrator to move the particles along the lattice. Some statistical considerations are given to justify the values used for the number of particles $N$ and the number of grid points $K$ on each dimension.

### 3.1 Initial distribution

The initial distribution is computed by mapping the hyper-ellipsoid in the 4D transverse phase (KV) and the disc in the 2D longitudinal phase (Neuffer), see equation (7), into a unit 3D cube and a unit square where the distribution is uniform. We use a random number generator to fill the 5D hypercube with N macro-particles, whose coordinates are mapped back to the 6D phase space. Introducing polar coordinates in any phase plane $X = r_x \cos(2\pi\,\phi_x)$ and $P_x = r_x \sin(2\pi\,\phi_x)$ where $0 \le \phi_x \le 1$ the hyper-ellipsoid is parameterized by $r_x = \sqrt{t\,\epsilon_{x0}}\cos\theta$ and $r_y = \sqrt{t\,\epsilon_{y0}}\sin\theta$ where $0 \le \theta < \pi/2$. Setting $\cos^2\theta = u$ where $0 \le u \le 1$ the transformation becomes

$$X = \sqrt{t\,u\,\epsilon_{x0}}\,\cos(2\pi\phi_x) \qquad Y = \sqrt{t\,(1-u)\,\epsilon_{y0}}\,\cos(2\pi\phi_y)$$

$$P_x = \sqrt{t\,u\,\epsilon_{x0}}\,\sin(2\pi\phi_x) \qquad P_y = \sqrt{t\,(1-u)\,\epsilon_{y0}}\,\sin(2\pi\phi_y) \tag{10}$$

In a similar way we introduce the transformation

$$Z = \sqrt{\epsilon_{z0}\,(1-v^{2/3})}\,\cos(2\pi\phi_z)$$

$$P_z = \sqrt{\epsilon_{z0}\,(1-v^{2/3})}\,\sin(2\pi\phi_z) \tag{11}$$

for the longitudinal coordinates One can check that $\rho\,dX\times$ $\times dY\,dZ\,dP_x\,dP_y\,dP_z = \delta(1-t)\,t\,dt\;du\,dv\,d\phi_x\,d\phi_y\,d\phi_z$. As a consequence after integrating over $t$, the distribution in $\phi_x, \phi_y, \phi_z, u, v$ is uniform on the unit 5D hypercube, and (10, 11) evaluated for $t = 1$ gives the distribtion in the original coordinates.

### 3.2 The Poisson solver

Given an arbitrary distribution of macro-particles with unit total charge, the calculation of the electric field is carried out by solving the Poisson equation with a spectral method. Assuming the center of the charge distribution to be at the origin we construct the parallelepiped $\mathcal{P} : |x| \le L_x,\ |y| \le L_y,\ |z| \le L_z$ whose sides are significantly larger than the corresponding rms radii $r_i$. (five times at least). We divide the $x$ side into $K_x = 2^{n_x}$ subintervals of length $\Delta x = 2L_x/K_x$ and, performing the same subdivision of the $y$, $z$ sides, we obtain a partition of the rectangle into a lattice of identical cells. The grid points are labelled by a vector $\mathbf{q} = (q_x, q_y, q_z)$ whose components are integer numbers and we denote their cartesian coordinates by $x(q_x), y(q_y), z(q_z)$ where $x_i(q_i) = L_i(-1+2q_i/K_i)$ and $q_i = 0, 1, .., K_i \equiv 2^{n_i}$ for $i = x, y, z$. If the bunch dimensions are comparable the choice $K_x = K_y = K_z = K$ is made. The density at each lattice point is given by $\rho = \Delta N/N$ where $\Delta N$ is the number of point-like macroparticles falling into a shifted cell whose center is at the given point, see figure 2, and $N$ is the total numer of macroparticles used in the simulation. This corresponds to the nearest grid point (NPG) interpolation for the charge deposition, see [12]. We can treat a macroparticle also as a uniform cloud of charge uniformly distributed in a parallelepiped of sides $\Delta x$, $\Delta y$, $\Delta z$ whose center is at the macroparticle position $(x, y, z)$. The contribution to the density at a grid point $x(q_x), y(q_y), z(q_z)$ is given by the sum of the macroparticles clouds intersecting the cell centered at the grid point, which is a paralleleped of sides $\Delta x$, $\Delta y$, $\Delta z$. In this case $\rho = \Delta N/N$, where each macroparticle at $(x, y, z)$ such that $|x - x(q_x)| < \Delta x$, $|y - y(q_y)| < \Delta y$ and $|z - z(q_z)| < \Delta z$ contributes with a weight $w$, namely $\Delta N = \sum w$, where

$$w = \left(1 - \frac{|x - x(q_x)|}{\Delta x}\right)\left(1 - \frac{|y - y(q_y)|}{\Delta y}\right)\left(1 - \frac{|z - z(q_z)|}{\Delta z}\right)$$

The Fourier expansion of $\rho$ and $V$ into a Fourier series allows an immediate solution of the Poisson equation

$$\begin{pmatrix}\rho\\ V\end{pmatrix} = \sum_{\mathbf{k}} \begin{pmatrix}\rho_{\mathbf{k}}\\ V_{\mathbf{k}}\end{pmatrix} \sin\left(\frac{\pi k_x}{L_x}x\right)\sin\left(\frac{\pi k_y}{L_y}y\right)\sin\left(\frac{\pi k_z}{L_z}z\right) \tag{12}$$

because they are related by

$$V_{\mathbf{k}} = \frac{4}{\pi}\,\rho_{\mathbf{k}}\,\left(\frac{k_x^2}{L_x^2}+\frac{k_y^2}{L_y^2}+\frac{k_z^2}{L_z^2}\right)^{-1} \tag{13}$$

The use of the FFT allows to obtain $V$ starting from $\rho$ at the grid points. Assuming for simplicity an equal number of subdivisions along all the axis and letting $K = 2^{n_x}$ the computational complexity is $(K\log K)^3$. The use of FFT in 2 dimension plus the inversion of three-diagonal matrix allows to lower the complexity to $K^3(\log K)^2$. We recall that spectral smoothing ($K$ finite) regularizes a field which would be singular, being generated by a finite number $N$ of point macroparticles. Indeed since PIC is an approximation scheme to solve the equations (3-5), we should first let $N$ and then $K$ go to infinity to converge to their solution. The electric field is then computed as a symmetric difference namely

$$E_x(q_x,q_y,q_z) = -\frac{V(q_x+1,q_y,q_z)-V(q_x-1,q_y,q_z)}{2\Delta x} \tag{14}$$

where for brevity we set $V(\mathbf{q}) \equiv V(x(q_x),y(q_y),z(q_z))$. To evaluate the field at the point where each particle is located an interpolation is required. We use a multilinear method. In 2D the algorithm consists in selecting the cell to which the point belongs, to interpolate linearly on two opposite sides and then on the line orthogonal to them. More explicitly letting $(q_x,q_y)$ be the a lattice point such that $x(q_x)\le x < x(q_x+1)$, $y(q_y)\le y < y(q_y+1)$ the algorithm reads

$$\begin{aligned} E_x(x,y) &= E_x(x,q_y)+\\ &+\frac{E_x(x,q_y+1)-E_x(x,q_y)}{\Delta y}\,(y-y(q_y))\\ E_x(x,q_y+n) &= E_x(q_x,q_y+n)+ \qquad n=0,1\\ &+\frac{E_x(q_x+1,q_y+n)-E_x(q_x,q_y+n)}{\Delta x}\,(x-x(q_x)) \end{aligned} \tag{15}$$

In 3D after interpolating the field in the planes $z(q_z)$, $z(q_z+1)$ a last interpolation in $z$ is carried out. Even though the result depends on the order in which the planes are chosen, the difference is of higher order with respect to the interpolation error.

**Boundaries** The numerical procedure can be extended to allow for the potential to vanish on the boundary of a connected domain $D\subset\mathcal{P}$. The method we describe

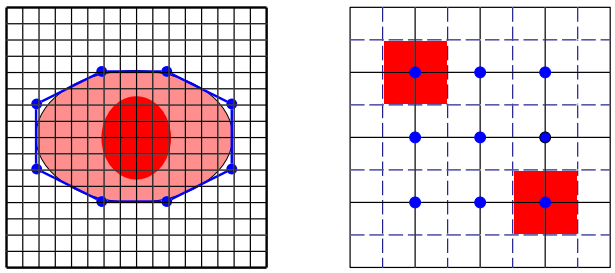

**Fig. 2.** Grid for a 2D charge distribution, with a polygonal approximation to the boundary (left). Conjugate lattice (dashed lines) for the computation of the density at the grid points (right)

is similar to the *capacity matrix method* [23]. First we solve the Poisson equation with Dirichelet condition on the boundary of $\mathcal{P}$

$$\Delta V_0 = -4\pi\rho \qquad V_0 = 0 \quad \text{on} \quad \partial\mathcal{P} \tag{16}$$

Then we choose a sequence of $K$ grid points $\mathbf{x}_j$ which are the vertices of a polygon $D_{\text{pol}}$ which approximates $D$, see figure 2, and compute the Green's functions

$$\Delta G_k = \begin{cases} 0 & \text{if} \quad \mathbf{x}\neq\mathbf{x}_k \\ 1 & \text{if} \quad \mathbf{x}=\mathbf{x}_k \end{cases} \qquad G_k = 0 \quad \text{on} \quad \partial\mathcal{P} \tag{17}$$

Then we build the function

$$V(\mathbf{x}) = V_0(\mathbf{x}) + \sum_{k=1}^{K}\alpha_k G_k(\mathbf{x}) \tag{18}$$

where obviously $V$ is a solution of the given Poisson equation in the interior of the polygon $D_{\text{pol}}$. In order to impose that $V$ vanishes at the vertices of the polygon we solve a linear system

$$V_0(\mathbf{x}_j) + \sum_{k=1}^{K}\alpha_k G_k(\mathbf{x}_j) = 0 \tag{19}$$

The inversion of the matrix $G_k(\mathbf{x}_j)$ needs to be made only at the beginning since it does not depend on $\rho$, but only on the boundary. In order to have an error of order $1/K^2$ an interpolation may be carried out. The method has been implemented in the $2D$ problem but its extension to 3D does not rise any problem except for the size of the set of linear equations to solve.

### 3.3 Discretization parameters

Choosing $K$ Fourier components in each dimension amounts to cover the $d$ dimensional cube $\mathcal{P}$ of side $2L$ with cells of side $\Delta x = 2L/K$. The number of cells which cover the domain $D$ is given by

$$n_C = \frac{\text{Vol}(D)}{(\Delta x)^d} = K^d\,\eta \qquad \eta = \frac{\text{Vol}(D)}{(2L)^d} \tag{20}$$

and for a uniform distribution of $N$ particles in $D$ the average number of particles per cell is $n_{_P} = N/n_{_C}$. Our first choice of the discretization parameters was obtained by requiring that the uncertainty in the position $\Delta x/\ell$ where $\ell = [\mathrm{Vol}(D)]^{1/d}$ should be equal to the statistical fluctuation $\Delta n_{_P}/n_{_P} = n_{_P}^{-1/2}$ of the number of particles. This choice, leads to a higher number of particles with respect to a standard choice of a few particles (typically 10 with CIC charge deposition) per cell

$$N = K^{d+2}\,\eta^{1+2/d} \qquad\qquad N_{\,\mathrm{stand}} = 10\,n_{_C} = K^d\,10\,\eta$$

In dimension $D = 2$ with $\eta = 10^{-2}$ using $K = 128$ the optimal number would be $N = 2.5 \times 10^4$ and the number of particles per cell $n_P \sim 150$ whereas $N_{\,\mathrm{stand}} = 1.3\times 10^3$. For our higher choice of $N$ the results do not change appreciably changing from NPG to CIC charge deposition method. As a consequence we believe that our very conservative choice allows to reduce strongly the self forces effects for NPG charge deposition. In the 3D model defined in section 1 the ratio of the volumes is $\eta = 0.009$, see caption of figure 4. As a consequence for $K = 64$ we would have $4 \times 10^5$ corresponding to $n_{_C} \sim 2 \times 10^3$ cells and $n_P \sim 160$ particles per cell. The standard choice would be $N_{\,\mathrm{stand}} = 2.5 \times 10^4$. Even in this case the higher number of particles chosen justifies the use of the NPG charge deposition method. We notice that the computational complexity of the linear evolution, field interpolation and the density evaluation is $\sim 200N$ and consequently since the field computational complexity is $K^3(9 + \log^2 K)$ namely $7 \times 10^6$, the load of the dynamical step and the Poisson solver is comparable for $K = 64$ and $N = 10^5$. A typical run over $10^3$ FODO cells requires about one day on a R10000 MIPS processor of an OCTANE workstation of Silicon Graphics. Increasing $N$ and $K$ to higher values requires a parallel implementation of the code, which has already been developed [24]. We have compared for $K = 64$ the results obtaining by decreasing the particle number to $2.5 \times 10^4$ and the difference in the averaged variables, radii and emittances, was always below 1%. The numerical stability with respect to variations in the number $K$ of Fourier components was also checked. As a consequence we believe that the results of the PIC simulations for the chosen values of $N$ and $K$ are reliable and numerically balanced.

### 3.4 Error in the electric field

The main problem in the simulation is that a self consistent solution is not known. We used a KV-Neuffer distribution in phase space which produces a distribution in a cylinder parabolic in $z$ according to (7). The discrepancy between the electric field generated by the KV-Neuffer and a uniform distribution in the ellipsoid

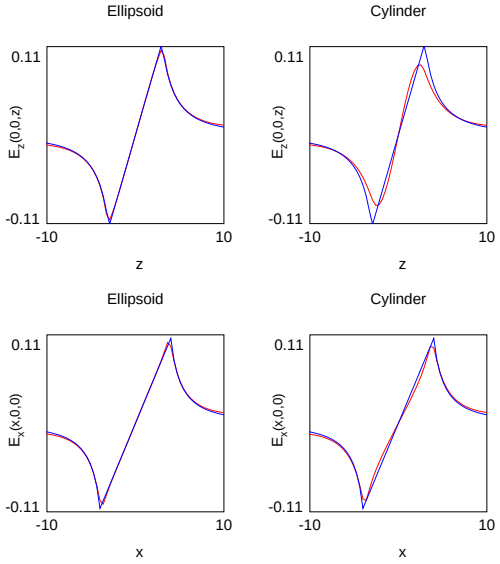


**Fig. 3.** Top: electric field component $E_z(0, 0, z)$ for a uniform unit charge on an ellipsoid $A_x = 4, A_y = 2, A_z = 3$ (left) and on a cylinder (right) according to (7). Bottom: The same for $E_x(x, 0, 0)$. The units are arbitrary: if the coordinates $x, y, z$ are in mm the electric field unit is $\mathrm{mm}^{-2}$. The red curve refers to the solution obtained with the Poisson solver for $K = 64$, the blue one to the analytical solution for the ellipsoid

with the same semi-axis is significant only near $z = \pm A_z$, as shown by figure 3. The discrepancy decreases by approaching the origin, see figure 3, where we plot the results for $A_x = 4$, $A_y = 2$, $A_z = 3$. The exact solution for the ellipsoid is computed by using the analytical results given in the next section, equation (33), where the elliptic integrals are evaluated by Gaussian quadratures to the desired accuracy. We choose a cube of half side $L = 11.5$ and define the error as $\left[(3K^3)^{-1}\sum_{\mathbf{q}} \|\mathbf{E}(\mathbf{q}) - \mathbf{E}_{\,\mathrm{ex}}(\mathbf{q})\|^2\right]^{1/2}$ where $\mathbf{q}$ runs on the lattice points. The relative errors for $K = 64$ are of the order of 1% (ellipsoid) and 10% (cylinder) respectively. For the cylinder, the major contribution is due to the $z$ component. The results obtained with $10^5$ particles randomly distributed in the ellipsoid or cylinder rather than with analytical density do not change appreciably.

The electric field generated by a macroparticle system with an initial KV-Neuffer distribution, changes as the system evolves but the deviations from the initial values are modest even for high values of the perveance. In figure 4 the results of a simulation with $\xi = 10$ are shown.

### 3.5 Evolution scheme

We have chosen a second order symplectic scheme for the dynamic evolution. The Hamiltonian (1), which depends on $s$, can be written as $H = H_0 + \frac{1}{2}\xi V$ where $H_0$ is the quadratic part and $\frac{\xi}{2}V$ is the space charge potential. The lattice Hamiltonian $H_0$ is a piecewise constant function of

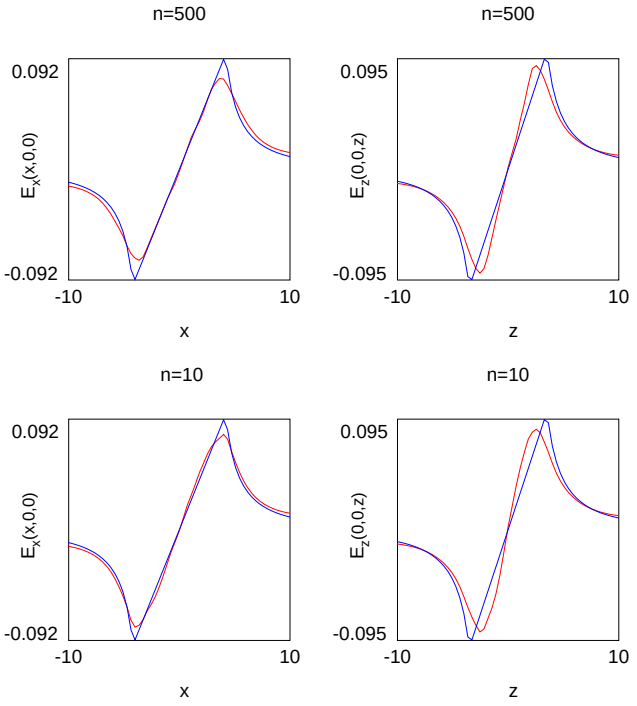


**Fig. 4.** Top: electric field components $E_x(x,0,0)$ (left) and $E_z(0,0,z)$ (right) after crossing 500 cells. Bottom: the same after crossing 10 cells. The electric field, corresponding to a unit charge, is is obtained from a PIC simulation with $\xi = 10$, $K = 64$, $N = 10^5$, $n_{\text{map}} = 48$; if $x, y, z$ are expressed in mm. the field unit is $\text{mm}^{-2}$. The red curves refer to the results of the simulations the blue curve to the field of a unit charge uniformly distributed on an ellipsoid with semi-axis $A_x = \sqrt{\beta_x \epsilon_{x0}} = 4.2, A_y = 1.78, A_z = 3.51$ mm. The side of the cube where the field is computed is $2L = 23$ mm.

$s$ whereas $V$ is continuous. The numerical scheme consists in treating the space charge force as an impulsive force namely to replace $H$ with

$$H_{\text{kick}} = H_0(s) + \frac{\xi}{2} \sum_{i=1}^{\infty} (s_{i+1} - s_i)\, \delta(s - s_i)\, V(s) \quad (25)$$

The set of points $s_i$ must include the discontinuity points of the quadrupolar gradients $k(s)$, $k_C(s)$. We illustrate the choice of the non uniform integration step for a lattice of identical FODO cells of length $\ell_{\text{tot}}$. First we choose an average step $\Delta s$ and divide the element $j$ of length $\ell_j$ into $n_j = [\ell_j/\Delta s]$ identical intervals of length $\Delta s^{(j)} = \ell_j/n_j$. The function $[x]$ is equal to the integer part and of $x$ if $x \geq 1$, to 1 if $0 < x < 1$. Choosing $\Delta s = \ell_{\text{tot}}/50$ for the lattice defined in table 2 we obtain a partition into 48 microcells of which 4 are identical to the active elements (one focusing, one defocusing, two RF cavities) the remaining 44 being just 1/11 of the drift length.
We recall that given a Hamiltonian $H = H_0 + V$ (set $\xi = 2$) independent of $s$ in the interval $[s_i, s_{i+1}]$ of length $\Delta s_i$ the evolution is given by a symplectic map $\mathbf{x}(s_{i+1}) = \mathsf{M}_{s_{i+1},s_i}\mathbf{x}(s_i)$ where $\mathsf{M} = e^{\Delta s_i\, D_H}$ is the Lie series and $D_H$ is the Lie operator whose action on any dynamic variable is the Poisson bracket $D_H A = [A, H]$. One can easily check that the ordinary splitting

$$\mathsf{M}_{s_{i+1},s_i} = e^{\Delta s_i\, D_{H_0}}\ e^{\Delta s_i\, D_V} + O\big((\Delta s_i)^2\big) \quad (26)$$

is a second order scheme, whereas the symmetric splitting

$$\mathsf{M}^{\text{sym}}_{s_{i+1},s_i} = e^{\frac{1}{2}\Delta s_i\, D_V}\ e^{\Delta s_i\, D_{H_0}}\ e^{\frac{1}{2}\Delta s_i\, D_V} + O\big((\Delta s_i)^3\big) \quad (27)$$

is of order 3. These schemes correspond to the exact evolution of the impulsive Hamiltonian $H^{(i)}_{\text{kick}} = H_0 + V\Delta s_i[\delta(s - s_i) + \delta(s - s_{i+1}]$. More precisely the second order approximation in (26) corresponds to the evolution defined by $H^{(i)}_{\text{kick}}$ from $\mathbf{x}(s_i - 0)$ to $\mathbf{x}(s_{i+1} - 0)$, the same approximations with the operators interchanged to the evolution from $\mathbf{x}(s_i + 0)$ to $\mathbf{x}(s_{i+1} + 0)$, the third order symmetric scheme (27) to the evolution from the $\mathbf{x}(s_i)$ to $\mathbf{x}(s_{i+1})$ defined as the averages of the left and right limits (recall that the integration of $\delta(s - s_i)$ starting from $s_i$ gives $\frac{1}{2}$). Partitioning the cell into $n$ microcells of average length $\Delta s = \ell_{\text{tot}}/n$ the error with the symmetric algorithms is $n\,(\Delta s)^3 = O(n^{-2})$. The Hamiltonian (25) gives the same contribution as (26) where $V$ is replaced by $V(s_i)$ to the evolution in $[s_i, s_{i+1}]$, whereas the symmetric evolution (27) becomes

$$\mathsf{M}^{\text{sym}}_{s_{i+1},s_i} = e^{\frac{1}{2}\Delta s_{i+1}\, D_{V(s_{i+1})}}\ e^{\Delta s_i\, D_{H_0}}\ e^{\frac{1}{2}\Delta s_i\, D_{V(s_i)}} \quad (28)$$

The symmetric evolution along the FODO cell gives

$$\mathsf{M}^{\text{sym}}(s_0, s_n) = e^{\frac{1}{2}\Delta s_n D_{V(s_n)}}\, M(s_0, s_n) e^{-\frac{1}{2}\Delta s_0 D_{V(s_0)}} \quad (29)$$

Recalling that the periodicity implies $\Delta s_n = \Delta s_0$ we notice that if the beam is matched, $V(s)$ is periodic of period $\ell_{\text{tot}}$, the errors for the symmetric and unsymmetric algorithm is the same since $V(s_n) = V(s_0)$ and the corresponding evolution operators are conjugated.

## 4 The particle in core model

The PC model is defined by the Hamiltonian (1) but the charge of the bunch is chosen to be uniformly distributed on an ellipsoid of semi-axis $A_x, A_y, A_z$. With this constraint the equations of motion for a macro-particle within the bunch are linear.

### 4.1 The envelope equation

We have computed iteratively the optical functions of these equations [25,10]. At the first step we set $V = 0$ obtaining the bare optical functions and the bare amplitudes. At the second step the potential $V$ is computed for an ellipsoid having the bare amplitudes as semi-axis. The new optical functions $\beta_{x1}, \alpha_{x1}, \ldots$ and amplitudes $A_{x1} = (\epsilon_{x0}\beta_{x1})^{1/2}, \ldots$ are determined and the process is iterated until convergence. The matched amplitudes and optical functions are related by (6). Up to $\xi = 10$ the method

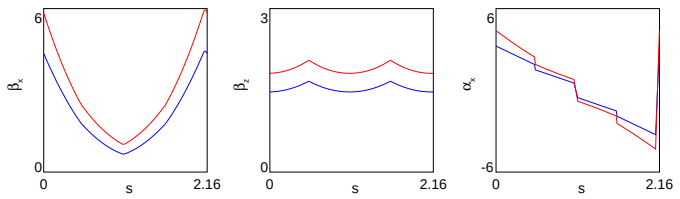


**Fig. 5.** Optical functions for $\xi = 0$ (blue curve) and for $\xi = 10$ (red curve) expressed in m.

can be safely used and one can show that the result is the same as the periodic solution of the envelope equations corresponding to the Hamiltonian

$$H_{\text{env}} = \frac{p_{A_x}^2 + p_{A_y}^2 + p_{A_z}^2}{2} + \frac{\epsilon_{x0}^2}{2A_x^2} + \frac{\epsilon_{y0}^2}{2A_y^2} + \frac{\epsilon_{z0}^2}{2A_z^2} + k(s)\frac{A_x^2 - A_y^2}{2} - k_C(s)\frac{A_x^2 + A_y^2}{4} + k_C(s)\frac{A_z^2}{2} + \frac{\xi}{2}V_{\text{env}}\ (\mathbf{A}) \tag{30}$$

where $V_{\text{env}}$ is the envelope potential defined by $dV_{\text{env}} = A_x\, c_x\, dA_x + A_y\, c_y\, dA_y + A_z\, c_z\, dA_z$ and $V = \frac{1}{2}(c_x\, x^2 + c_y\, y^2 + c_z\, z^2)$ is the potential inside the ellipse. If the electric field components are $E_i = c_i(\mathbf{A})x_i = -\partial V/\partial x_i$, defined by (33) in subsection 4.2, then the corresponding force in the envelope equation is $-\partial V_{\text{env}}/\partial A_i = c_i(\mathbf{A})A_i$.

| $\xi$ | $\omega_x$ | $\omega_y$ | $\omega_z$ | $\beta_x$ | $\beta_y$ | $\beta_z$ |
|---|---|---|---|---|---|---|
| 0 | 84 | 84 | 81 | 4.38 | 0.670 | 1.47 |
| 5 | 69 | 69 | 72 | 5.07 | 0.850 | 1.65 |
| 10 | 58 | 58 | 65 | 5.85 | 1.03 | 1.81 |

TABLE 3 Phases (in degrees) and optical functions in m. at $s = 0$

Unlikely the 2D case the density $\rho_s$ of the PC model is not the projection of a phase space distribution $\rho$, self consistent solution of the Poisson-Vlasov equations (1,3). The self consistent distribution $\rho$ corresponding to (7) has a projection $\rho_s$ which differs moderately from the PC distribution as illustrated in section 3.4.

In absence of space charge the optical functions are computed exactly, at the lattice points $s_i$, defined in Section 3.5.

After computing the cell map $\mathsf{L}(0) = \mathsf{L}_1 \cdots \mathsf{L}_{n\ \text{map}}$ at $s = 0$ as a product of all the micro-maps, the recurrence $\mathsf{L}(s_i) = \mathsf{L}_i\, \mathsf{L}(s_{i-1})\, \mathsf{L}_i^{-1}$ allows to obtain the cell map $\mathsf{L}(s_i)$ at the location $s_i$ and to determine the optical functions there. When the space charge is present, its contribution is a linear kick and the cell map is evaluated in the same way. The iterative procedure described above allows to determine the sequence $A_{x\,n}, \beta_{x\,n}, \alpha_{x\,n}$ which converges below a critical value of $\xi$. The only error in this case is the discretization of the space charge force. We find that with $n_{\text{map}} = 48$ an accuracy better than $10^{-3}$ is obtained on the tune shifts and the optical functions. In table 3 we quote the phase advance and $\beta$ for the bare cell and the cell with space charge with $\xi = 10$. In figure 5 we show the graphs of the optical functions for the bare cell and the cell with space charge.

### 4.2 Electric field computation

The electric field generated by a uniform distribution in an ellipsoid is known exactly up to an integration [27, 28], which can be performed in terms of elliptic functions or, more conveniently, with Gaussian quadratures after a suitable change of variables. Letting $A_x, A_y, A_z$ be the ellipsoid semi-axis we define for $s \geq 0$

$$D(s) = (A_x^2 + s)\ (A_y^2 + s)\ (A_z^2 + s)$$
$$\lambda(s; x, y, z) = \frac{x^2}{A_x^2 + s} + \frac{y^2}{A_y^2 + s} + \frac{z^2}{A_z^2 + s} \tag{31}$$

If the point of coordinates $(x, y, z)$ is interior or exterior to the ellipsoid $1 - \lambda(0; x, y, z)$ is positive and negative respectively; moreover we have $\lambda(s; x, y, z) < \lambda(0; x, y, z)$. We introduce the function $\chi(x, y, z)$ defined as $\chi = 0$ if $\lambda(0; x, y, z) \leq 1$ and otherwise as the unique real positive solution $\chi$ of a cubic equation in $s$ defined by $\lambda(s; x, y, z) = 1$. When the point is exterior and $\chi > 0$ then $A_i' = (A_i^2 + \chi)^{1/2},\ i = x, y, z$ are the semi-axis of the confocal ellipsoid. Given a unit charge distributed on the ellipsoid with a density $\rho$ depending only on $\lambda$, the potential and the electric field are given by

$$V = \pi\, A_x A_y A_z \int_0^\infty \frac{\mu(\lambda)\, \vartheta(1 - \lambda)}{\sqrt{D}}\, ds$$
$$E_i = 2\pi\, x_i\, A_x A_y A_z \int_0^\infty \frac{\rho(\lambda)\, \vartheta(1 - \lambda)}{(A_i^2 + s)\sqrt{D}} ds \tag{32}$$

where $\mu(\lambda) = \int_\lambda^1 \rho(t)\, dt$. The potential and the field corresponding to a charge distribution on an infinite cylinder with elliptical cross section is obtained by taking the limit $A_z \to \infty$. We consider here the case of constant density $\rho(\lambda) = \rho_0,\ \mu(\lambda) = (1 - \lambda)\rho_0$ where $\rho_0^{-1} = \frac{4}{3}\pi\, A_x A_y A_z$. Since for interior points $\lambda(s) < 1$ for any $s \geq 0$, whereas for exterior points $\lambda(s) < 1$ if $s > \chi$ we obtain

$$V = \frac{3}{4} \int_{\chi(x,y,z)}^\infty \frac{1 - \lambda(s; x, y, z)}{\sqrt{D(s)}}\, ds$$
$$E_i = \frac{3}{2}\, x_i \int_{\chi(x,y,z)}^\infty \frac{1}{(A_i^2 + s)\sqrt{D(s)}}\, ds \tag{33}$$

Since $\chi = 0$ for the interior points, the electric field there is linear. In order to carry out the integration we perform a change of coordinates $s \to u$ which brings the integration to a finite interval $[0, u_0]$ and removes the singularity at $u = 0$

$$s = A_x A_y \left(\frac{1}{u^\alpha} - 1\right) \qquad u_0 = \left(1 + \frac{\chi}{A_x A_y}\right)^{-1/\alpha} \tag{34}$$

Choosing $\alpha = 3/2$ for $E_i$ the integral is regularized and a Gaussian integration gives a very accurate result. The potential $V$ splits into two integrals: for the first one, whose integrand has a numerator 1, we choose $\alpha = 2$, for the second with numerator is $\lambda$ we choose $\alpha = 3/2$. We have checked the accuracy of the integration with 4 Gaussian points, propagated in subintervals of $[0, u_0]$ against the analytical expressions for a symmetric ellipsoid $A_y = A_x$. The use of $32 \times 4$ Gauss points is adequate.

## 5 Analysis of the results

We describe here the results obtained on two numerical experiments carried out with intermediate and high space charge namely $\xi = 5$ and $\xi = 10$ (this is the value since we measure $s$ in m, $x, y, z$ in mm and the emittance in mm mrad. Measuring $x, y, z$ in m and the emittance in in m rad the perveance would be multiplied by $10^{-9}$). The electric field has moderate variations, as shown by figure 4, where we compare it with the PC field. The main feature is that the fields are almost linear within the core and the longitudinal field tends to be stronger within the core, with respect the ellipsoid case, as shown by figure 4, where $E_x(x, 0, 0)$ and $E_z(0, 0, z)$ are plotted after 10 cells and 500 cells. We notice that the region of linearity is smaller. This is due to the change in the structure of the core. After the first few cells the distribution changes considerably. We have analyzed its space projection in the $x, y$ plane and in the $z, p_z$ plane, see figure 6. In both cases we observe that, after a transient rearrangement, which is more dramatic in $z$ and smoother in $x, y$, the distributions take a similar shape, given by a central core and a tail of exponentially decreasing density.

It turns out consequently that they can be nicely fitted with a Fermi Dirac distribution, see figure 6

$$\rho_{FD}(t) = \frac{\alpha}{\log(1 + A^{-1})} \frac{1}{Ae^{\alpha t} + 1} \tag{35}$$

where the best-fitting parameters are stable after 200 cells and are $A = 0.16, \alpha = 3$ for the distribution in $t = x^2/A_x^2 + y^2/A_y^2$ and $A = 0.18, \alpha = 5$ for $\epsilon_z/\epsilon_{z0} = (Z^2 + P_z^2)/\epsilon_{z0}$. In figure 7 the plot of points in the transverse configuration space clearly shows the formation of a halo described by the Fermi-Dirac tail.
The main feature is that the rms radii and rms emittances have moderate variations. Short and long period oscillations are observed. The frequencies are determined by analyzing the signal $\langle x_n^2 \rangle^{1/2}$ and the corresponding ones for the $y$ and $z$ axis. The results are comparable: for short signals $0 \le n \le 32, 64$ two frequencies $\nu_1 = 0.390$ and $\nu_2 = 0.435$ and low frequency $\nu_s$ are found. The frequencies $\nu_1$ and $\nu_s$ are very stable and are found for the $x, y$ and $z$ signals, whereas $\nu_2$ appears in the $y$ or $z$ signal. For longer signals $1 \le n \le 128, 256, 512$ still $\nu_1$ and $\nu_s$ are present and their value is unchanged. We interpret

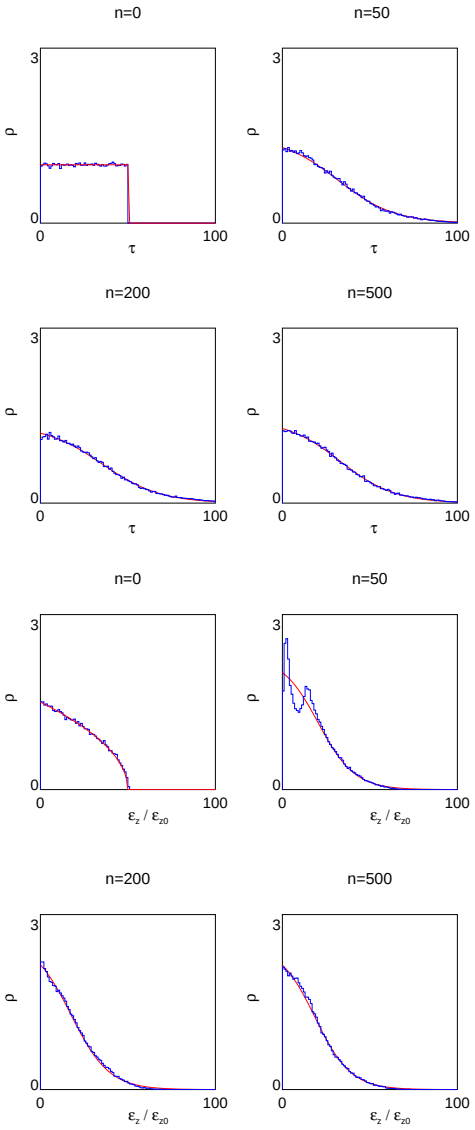


**Fig. 6.** Normalized distribution of $\tau = x^2/A_x^2 + y^2/A_y^2$ (top) $\epsilon_z/\epsilon_{z0} = (Z^2 + P_z^2)/\epsilon_{z0}$ (bottom) after $0, 50, 200, 500$ FODO cells. PIC simulation (blue), Fermi-Dirac fit for $n > 0$ (red)

the stable short frequency as a mismatch, even mode oscillation, which in the smooth approximation is given by $\nu_{1\ \mathrm{mis}} = 0.428$. The remaining mismatch frequencies are are $\nu_{2\ \mathrm{mis}} = 0.373$ and $\nu_{2\ \mathrm{mis}} = 0.366$. The origin of the low frequency oscillations, which are clearly observable in figure 8, for all the rms variables with period 40, still remains to be explained.

In figure 8 we show the plots of the rms quantities over 200 and 1400 turns obtained with the following parameters $K = 64,\ N = 10^5, n_{\ \mathrm{map}} = 48$.
Just to give an idea of the difference in the dynamical behavior of the PC model and the simulation, we have plotted the orbits of a few test particles within and out of the core for a variable length of the orbit, see figure 11.

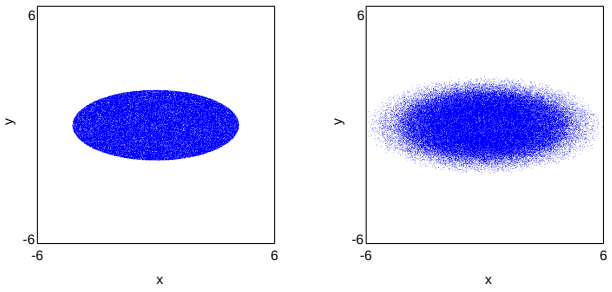


**Fig. 7.** Plot of points in the $x, y$ plane for $\xi = 10$ at the beginning (left) and after 10 cells (right). The $x, y$ unit is mm.

Up to a few hundred FODO cells the orbits are similar but at one thousand cells or more the differences become evident and some sort of diffusive behavior appears.
Nevertheless the overall behavior is not diffusive since the rms quantities have modest variations.
We have made a comparison with the PC model by computing the frequencies for a sequence of test particles chosen on the $X$ axis in the normalized coordinates and on an annular region in the $X, Y$ plane in order to plot the frequency map, which is effective in detecting the resonances between the betatron and collective oscillations.
In figure 9 we compare the transverse tunes for an orbit extending on 300 cells for two values of the perveance $\xi = 5, 10$. Out of the core the tunes are in reasonable agreement. Since the core is quite different from a uniform ellipsoidal charge distribution one can expect some dependence on the amplitude. We have also performed the frequency map analysis (FMA) [29,30] for a uniform grid of initial conditions in the $X, Y$ plane in an annular region between the core and twice its area, choosing $Z = 0$ and zero momenta $P_x = P_y = P_z = 0$, (see the caption of figure 10). The FMA turns out to be a useful tool to give a picture of the phase space of the PC model in the mismatched case. Regular trajectories define a regular mapping between the initial conditions and the frequency space; the uniform grid of initial conditions is smoothly deformed in the frequency space.

Resonant trajectories appear as a set of points clustering on a plane (line) in the frequency space (plane), surrounded by an empty channel.

The chaotic trajectories are sensitive to the initial conditions and form fuzzy clouds in the frequency space.
In figure 10 the plot in the $\nu_x, \nu_y$ plane for $\xi = 10$ shows that the main resonance structures are present both in the PIC simulation and the PC model. Then the effect of the mismatch was explored on the PC model using the FMA. In figure 12 we show the plots of the transverse and longitudinal tunes for a 10% mismatch, capable of exciting mainly the first mode.

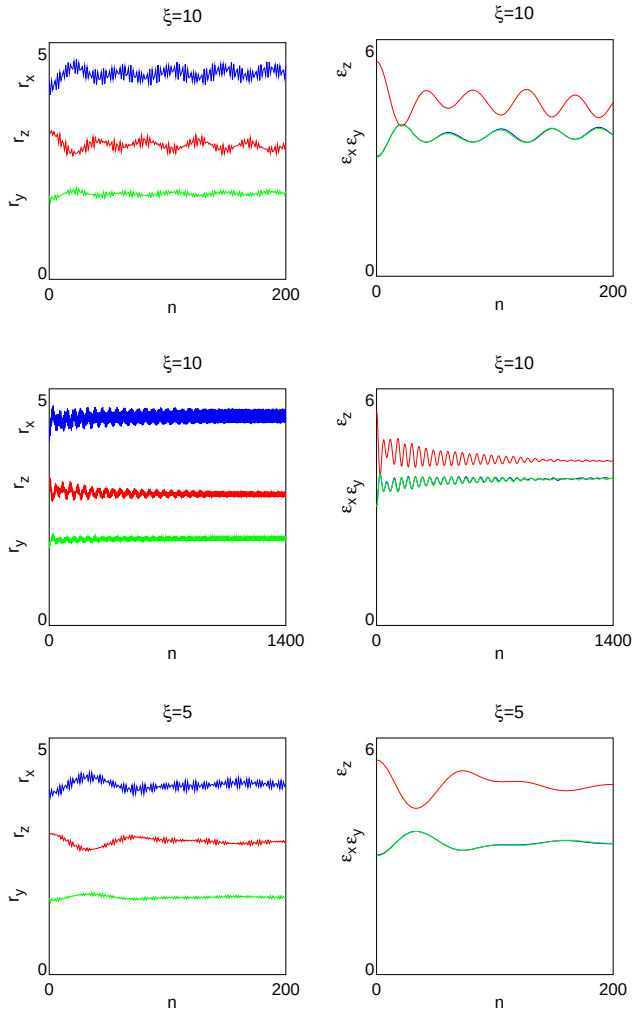


**Fig. 8.** Plot of the rms radii and emittances obtained from a PIC simulation with initial KV-Neuffer distribution using $K = 64$, $N = 10^5$, $n_{\text{map}} = 48$ for $\xi = 5, 10$. We denote by $n$ the number of cells crossed. The unit are mm for the rms radii and mm mrad for the rms emittances.

With the choice $A_x = 1.1\, A_{x\ \text{matched}}$ , $A_y = 0.9\, A_{y\ \text{matched}}$ , $A_z = A_{z\ \text{matched}}$ , a quadrupole mode is excited. The resonances in which the transverse frequencies are one half of the small mismatch oscillation frequencies $\nu_x = \nu_{x\ \text{mis}}\ /2$, $\nu_y = \nu_{y\ \text{mis}}\ /2$ are clearly recognized in the frequency plot. The initial condition corresponding to the resonant orbits are shown in figure 12 by using different colors. The application of the FMA to the study of 3D phase space of an ellipsoidal bunch has been considered [16].

## 6 Conclusions

We have examined a model for a linac with high current by considering the numerical solution of the Poisson-Vlasov

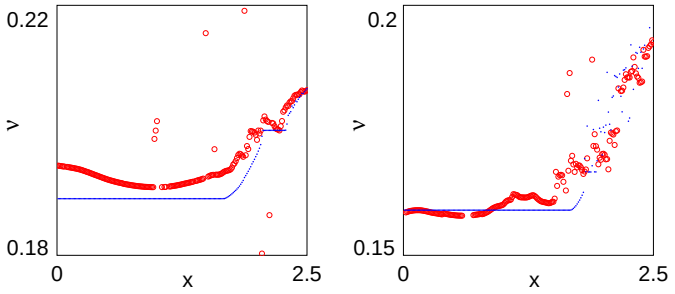


**Fig. 9.** Horizontal tunes obtained by FFT analysis of orbits extending on $n = 300$ FODO cells for $\xi = 5$ (left) and $\xi = 10$ (right). We compare the results of the PIC simulation (red circles) and the PC model (blue dots). The plot is against the normalized $X$ coordinates, the initial conditions being equidistributed in $0 < X \leq 2.5$ and $Y = Z = P_x = P_y = P_z = 0$ . The $X$ radius of the core is $R_x = \sqrt{\epsilon_{x\,0}} = 1.74$. Since $x$ and $\beta_x$ are measured in mm and m respectively, the units for $X, R_x$ are mm/m$^{1/2}$.

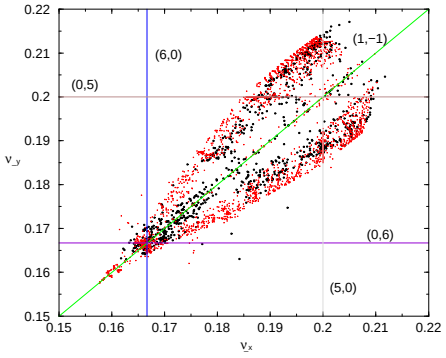


**Fig. 10.** Frequency plot: the results of the PIC simulation (black dots) for $\xi = 10$ is compared with the results of the particle in core model (small red dots). The initial conditions are chosen in the normal coordinates $X, Y$ plane in a ring $1 \leq X^2/A_x^2 + Y^2/A_y^2 \leq 2$. The length of the orbits is $n = 300$ FODO cells.

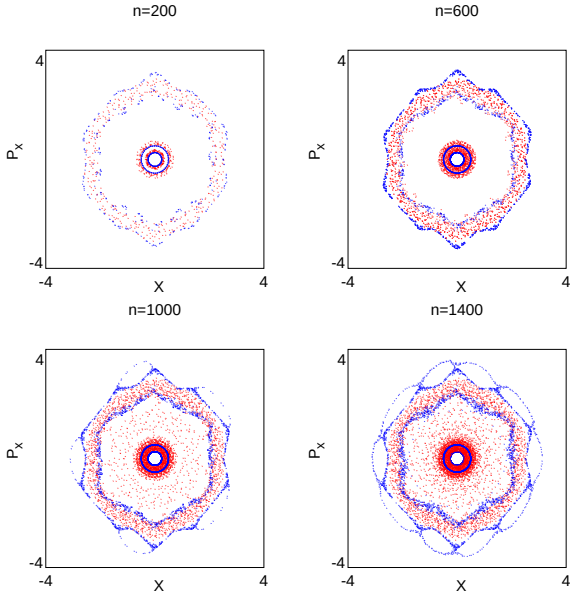


**Fig. 11.** Comparison of the orbits in the normal coordinates plane $X, P_x$ obtained from the PIC simulation and the PC model for 4 different initial conditions corresponding to $X = 0.25, 0.5, 2.25, 2.5$ and $Y = Z = P_x = P_y = P_z = 0$. The perveance is $\xi = 10$ and the radius of the core is $R_x = \sqrt{\epsilon_{x0}} = 1.74$. The various frames show the same orbits at various lengths corresponding to $n = 200, 600, 1000, 1400$ FODO cells. The blue points refer to the PC model the red points to the PIC simulation. The units are mm/m$^{1/2}$ since we measure the transverse coordinates in mm, the optical functions in m.

equations. The major problem is the lacking of an analytical self consistent solution to compare with and to test the accuracy of the numerical scheme. We have used a symplectic scheme for the dynamical evolution consisting in a kick approximation of the self field force on a sequence of micro-cells and a spectral method to solve the Poisson equation. Comparison with other 3D codes [31, 32] has been planned and performed at present just with Parmila [33]. The accuracy in the field computation has been checked in the static case. In the dynamic evolution we have chosen an initial KV-Neuffer distribution, which is not self consistent and which very rapidly evolves towards a distribution where the core is followed by Maxwellian tails and can be fitted with a Fermi-Dirac distribution. The core appears to be stable as shown by the rms quantities which have moderate variations and reach asymptotic values after $\sim 10^3$ FODO cells. On the contrary the departure from the initial distribution occurs after a few cells. The single particle emittances vary, which means that a re-mix of the particle within the core may occur. The PIC simulations described have been carried out on a FODO cell subdivided into $n_{\,\mathrm{map}} = 48$ micro-cells with a grid of $K^3$ cells with $K = 64$ and $N = 10^5$ macro-particles, and the stability of the results with respect to an increase of $n_{\,\mathrm{map}}$ and $N$ was verified. With these parameters the load of the dynamical evolution and the Poisson solver is comparable: increasing $K$ and $N$ is possible with the parallel implementation of the code. Nevertheless to investigate the linac problem where the number of cells is below 100, this appears not to be necessary. A comparison with the results of the PC model has shown that the dynamics are comparable for low $n$ (below 200), see figure 11, and the frequency analysis produces similar results: the same resonant structures appear. This means that the informations on the resonances and related stochastic regions due to space charge and mismatch oscillations are reliable for the purpose of a linac design. The exploration of the equilibrium asymptotic state of the system requires further investigations and more accurate experiments which will be carried out with the parallel implementation.

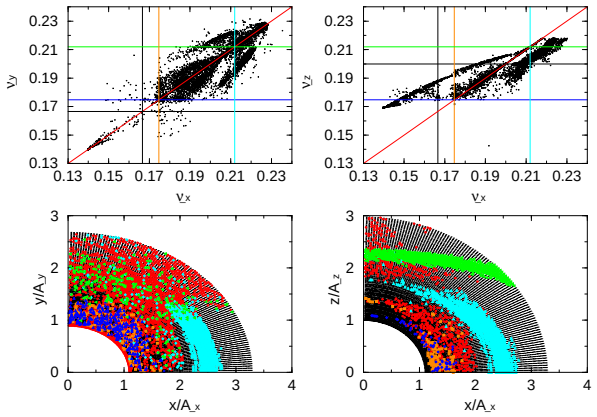


**Fig. 12.** FMA for 10% mismatch beam; in the upper graphs we have plotted the straight lines of the resonances $\nu_x = \nu_y$ and $\nu_a = \nu_b$ mis /2 $a = x, y$ $b = x, y, z$; the corresponding initial conditions are indicated by different marks in the lower graphs to point out the resonance overlapping.

**Acknowledgments** One of us, G. Turchetti, would like to thank G. Franchetti for useful discussions and to acknowledge CINECA for a grant, allowing to perform part of the computations described here and to develop a parallel version of the code on the T3D. S. Rambaldi would like to thank Prof. Orzag of MIT for useful suggestions.

## 7 APPENDIX

To justify the statistical analysis of the density and electric field fluctuations, subsection III-C, we present here a one dimensional model where the corresponding results are proved. Consider a uniform charge distribution of density $\rho$ in a slab between the planes $x = \pm L$ and let $Q = 2L\,\rho$ be the charge per unit area in the slab. The electric field is aligned with the $x$ axis and $E(x)$ satisfies $dE/dx = 4\pi\rho = 2\pi Q/L$ so that

$$E(x) = 2\pi\, Q\, \frac{x}{L} \quad |x| < L, \qquad E(x) = 2\pi\, Q\, \sigma(x) \quad |x| \geq L \tag{A1}$$

where $\sigma(x)$ denotes the sign of $x$.
The field within the slab is linear, just as the field within the the core for a 2D KV distribution or approximately for our 3D model. We consider a partition of the interval $|x| \leq L$ into a regular lattice with spacing $\Delta x = 2L/K$ for $K$ even. The points of the lattice are $x_k = k\,\Delta x$ for $|k| \leq K/2$ and to each point we associate the interval $I_k$ defined by

$$x \in I_k \qquad x_k - \frac{\Delta x}{2} \leq x \leq x_k + \frac{\Delta x}{2} \tag{A2}$$

see figure 13.

**Regular distribution** We replace then the given charge with of $N$ charged planes $x = x_i^*$ with a charge $q = Q/N$ per unit area or with a uniform charge distributions between the planes $x = x_i^* \pm \frac{1}{2}\Delta x$ having the same charge per

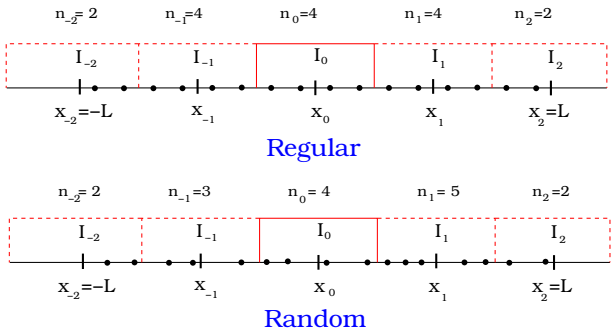


**Fig. 13.** Regular and random distribution of $N = 16$ points in $[-L, L]$ partitioned into $K = 4$ equal intervals by the lattice points $x_k, k = -2, \cdots, 2$. The Intervals $I_k$ centered at $x_k$ contain $n_k$ points.

unit area. We denote by $I_i^*$ the interval $x = x_i^* \pm \frac{1}{2}\Delta x$ From now on we refer to the charged planes as point charges and to the uniform distributions in the mini-slabs as clouds. The density for point charges is

$$\rho^*(x) = q \sum_{i=1}^{N} \delta(x - x_i^*) \tag{A3}$$

and the corresponding electric field is

$$E^*(x) = 2\pi q \sum_{i=1}^{N} \sigma(x - x_i^*) \tag{A4}$$

The clouds density $\rho^*(x)$ is obtained by replacing $\delta(x)$ with the step function $\delta_{\Delta x}(x) = 1/\Delta x$ if $|x| < \Delta x/2$.

**Space discretization** The analogue of the numerical procedure of space discretization consists in replacing the density $\rho^*(x)$ with a density defined at the lattice points $x_k$ as $\rho_k^* = q_k^*/\Delta x$ where $q_k^* = q n_k$ is the total charge in the interval $I_k$ and $n_k$ is the number of elementary charges. One has

$$\rho_k^* = \frac{1}{\Delta x} \int_{x_k - \frac{\Delta x}{2}}^{x_k + \frac{\Delta x}{2}} \rho^*(x) dx = q \sum_{i=1}^{N} S(x_k - x_i^*) \tag{A5}$$

where $S(x)$ is the square or triangular shape function defined in [5]: $S(x) = \delta_{\Delta x}(x)$ for point charges, $S(x) = (\Delta x)^{-1}(1 - |x|/\Delta x)$ if $|x| < \Delta x$ for the clouds. Rather than using a finite difference or FFT algorithm to find the field at the lattice points we associate to $\rho_k^*$ a density $\hat{\rho}(x)$ corresponding to point charges $q_k^* = \Delta x\, \rho_k^*$ located at the lattice points

$$\hat{\rho}(x) = \sum_{k=-K/2}^{k=K/2} q_k^*\, \delta(x - x_k) \tag{A6}$$

The corresponding electric field is

$$\hat{E}(x) = \sum_{k=-K/2}^{k=K/2} 2\pi\, q_k^*\, \sigma(x - x_k) \qquad (A7)$$

In the case of a regular distribution of $n_{_P}$ (even) equally spaced particles per interval ($N = K\, n_{_P}$) we have $\rho_k^* = n_{_P}\, q/\Delta x = \rho$ for $|k| < K/2$ and $\rho^*_{\pm K/2} = \rho/2$ and the electric field is

$$\hat{E}(x) = 2\pi\, n_{_P}\, q\, (2k{+}1) = 2\pi\, \frac{Q}{L}\left(x_k{+}\frac{\Delta x}{2}\right) \quad x_k < x < x_{k+1}$$

for $-K/2 \le k \le K/2 - 1$

$$\hat{E}(x) = \sigma(x)\, 2\pi\, n_{_P} q = \sigma(x)\, 2\pi Q \qquad |x| > L \qquad (A8)$$

The result is the same for a uniform distribution of $N$ clouds. We notice that in this case the field at $x_k$ is discontinuous with left and right limits $2\pi\, Q\, L^{-1}(x_k \pm \Delta x/2)$. Defining the field as the average $E_k = \frac{1}{2}(\hat{E}(x_k + 0) + \hat{E}(x_k - 0))$ at the inner points $|k| < K/2$ and $E_{\pm K/2} = \hat{E}(x_{\pm_{K/2}} \pm 0)$ at the ends, the exact result is recovered. The linear interpolation gives also the exact result.

**Random distribution** Consider the random generation on $N$ point charges $q = Q/N$ with a uniform probability in $[-L, L]$ and denote by $n_k$ the number of points which fall in the interval $I_k$, see figure 1. The charge in the interval $I_k$ is is $q_k^* = qn_k$ and the field $\hat{E}(x)$ generated by point charges $q_k^*$ at $x = x_k$ with density (A6) is given by (A7). Since $\hat{E}(x)$ is discontinuous at the $x_k$ we define its value $E_k$ there as the average of ledt and right limits if $|k| < K/2$ and the limit from outside at the ends if $k = \pm K/2$ so that

$$E_k = 2\pi q \left( \sum_{j=-K/2}^{k-1} n_j - \sum_{j=k+1}^{K/2} n_j \right) \quad \text{for} \quad |k| < \frac{K}{2} \qquad (A9)$$

At the end points the field is still $E_{\pm K/2} = \pm 2\pi Q$. For a regular distribution $n_k = qn_{_P}$ if $|k| < K/2$ and $n_{\pm K/2} = \frac{1}{2} q\, n_{_P}$, where $N = K\, n_{_P}$, the exact result $E_k = 2\pi Q\, x_k/L$ is recovered from (A9).

**Fluctuation estimates** In order to analyze the density and electric field fluctuations we consider the random variables

$$\rho_k = \frac{qn_k}{\Delta x} = \frac{Q}{N\Delta x} \sum_{i=1}^{N} \chi_{_{I_k}}(x_i^*)$$

$$E_k = \frac{2\pi Q}{N} \sum_{i=1}^{N} (\chi_{A_k}(x_i^*) - \chi_{B_k}(x_i^*)) \qquad (A10)$$

where $A_k = [-L, x_k]$, $B_k = [x_k, L]$ and $\chi_A(x)$ denotes the characteristic function of the set $A$. We have changed the lower index in the second sum in (A9) from $k + 1$ to $k$ since the results do not change appreciably for the statistical analysis and the computations are simpler. With this

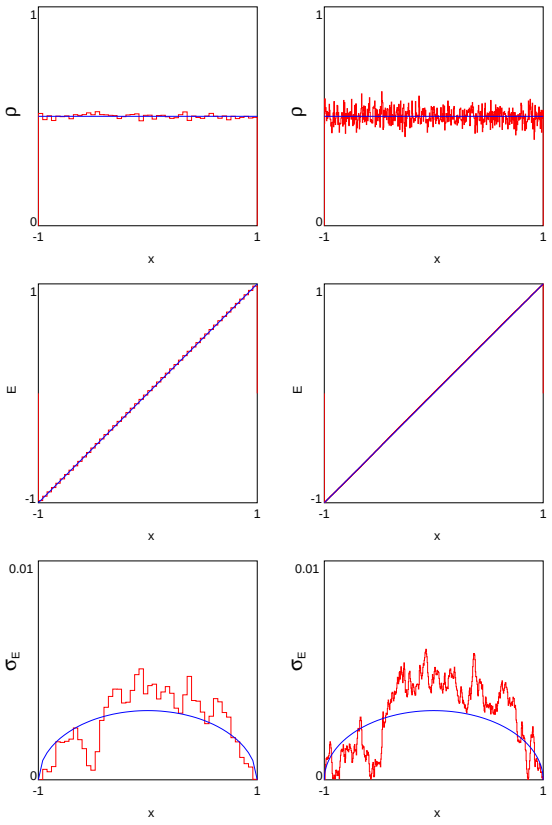


**Fig. 14.** Density and electric field dependence on the interval number $K$ for $N = 10^5$ randomly generated particles in the interval $[-1, 1]$. The figures on the left have $K = 50$, the figures on the right have $K = 500$. The top figures show the density histogram. The middle figures show the electric field. The bottom figures show the electric field variance. It is evident that the density fluctuations increase with $K$ whereas the electric field fluctuations are $K$ independent. The red curves refer to the simulation, the blue curves to the result.

change $E_k$ is $2\pi q$ times the difference between the number of particles falling in the intervals $A_k$ and $B_k$. The variables $x_i^*$ belong to $\mathbb{R}$ and their probability measure is $\mu(x) = (x + L)/2L$ if $x \in [-L, L]$, constant elsewhere. To evaluate the average and the variance of $\rho_k$ and $E_k$ defined in the product space $\mathbb{R}^N$ is standard in probability theory, For instance the electric field mean is

$$\langle E_k \rangle = \frac{2\pi Q}{N} \int \sum_{i=1}^{N} (\chi_{A_k}(x_i^*) - \chi_{B_k}(x_i^*))\, d\mu(x_1) \cdots d\mu(x_N) = 2\pi Q\, [\mu(A_k) - \mu(B_k)] = 2\pi Q\, \frac{x_k}{L} \qquad (A11)$$

In a similar way we evaluate

$$\langle E_k^2 \rangle = (2\pi Q)^2\, N^{-1}\, [1 + (N-1)(\mu(A_k) - \mu(B_k))^2] \qquad (A12)$$

so that the mean square deviation is

$$\sigma^2_{E_k} = \frac{(2\pi Q)^2}{N} \left(1 - \left(\frac{x_k}{L}\right)^2\right) \qquad (A13)$$

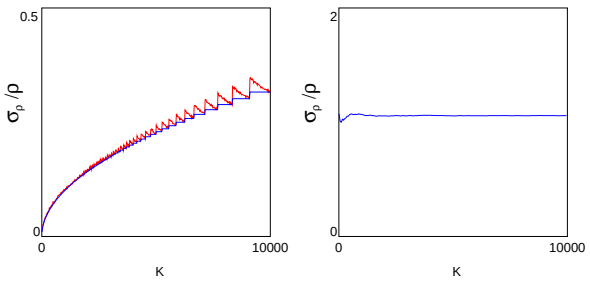


**Fig. 15.** Variation with the number number of intervals $K$ of the density fluctuation $\sigma_\rho/\rho$ (left) and of the electric field fluctuation $\sigma_E\sqrt{N}$ (right) for $N = 10^5$ randomly generated particles in $[-1, 1]$. The variance is averaged on all the intervals.

The mean density is given by

$$\langle \rho_k \rangle = \frac{Q}{\Delta x}\,\mu(I_k) = \frac{Q}{\Delta x}\,\frac{1}{K}$$

and its mean square value

$$\sigma^2_{\rho_k} = \left(\frac{Q}{\Delta x}\right)^2 \frac{\mu(I_k) - \mu(I_k)^2}{N} \sim \left(\frac{Q}{\Delta x}\right)^2 \frac{1}{N\,K} \qquad (A14)$$

The electric field variance $\sigma_{E_k}$ does not depend on $K$ whereas the density variance $\sigma_{\rho_k}$ does. The density fluctuation is

$$\frac{\Delta\rho_k}{\rho_k} = \left(\frac{K}{N}\right)^{1/2} = \frac{1}{\langle n_{_P}\rangle^{1/2}} \qquad (A15)$$

where $\langle n_{_P}\rangle$ denotes the average number of particles in each interval. The spread of the values of $\rho_k$ around the mean value is Gaussian with variance $\sigma_{\rho_k}$ according to the central limit theorem. The electric field fluctuation is

$$\frac{\Delta E_k}{|E_k|} = \frac{(1 - x_k^2/L^2)^{1/2}}{|x_k|/L}\,\frac{1}{\sqrt{N}} \le \frac{K}{2\sqrt{N}} \quad k \neq 0 \qquad (A16)$$

where the highest value is achieved close to the center at $x = \pm\Delta x$. The condition $\Delta\rho/\rho \sim 1/K$ gives $K = N^{1/3}$ and $\Delta E/E \sim N^{-1/6}$.

**Self forces** The choice $N = K^3$ makes a fluctuation of the electric field to zero unlikely even at $x = \pm\Delta x$. The self-force field contribution is dominated by the electric field of the remaining particles. Let us consider the field generated by a single particle or cloud located at $x^*$. Its contribution to the charge at the lattice points is $q^*_k = q\,\Delta x S(x_k - x_*)$ according to (A5). For the point charge the self field according to (A7) reads

$$\hat{E}(x^*) = 2\pi\,q \sum_{k=-\frac{K}{2}}^{k=\frac{K}{2}-1} \sigma(x_k + \frac{1}{2}\Delta x - x_*)\ \chi_{[x_k,x_{k+1}]}(x_*) \qquad (A17)$$

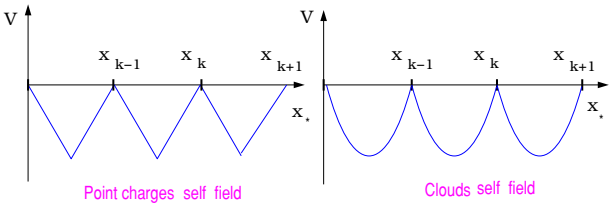


**Fig. 16.** Self field potential for point charges and clouds

and is piecewise constant; its potential is a sawtooth with minima at $x_k + \Delta x/2$, see figure 16. In the case of clouds the self field is

$$\hat{E}(x^*) = -2\pi q \sum_{k=-\frac{K}{2}}^{k=\frac{K}{2}-1} \frac{x_* - (x_k + \frac{1}{2}\Delta x)}{\frac{1}{2}\Delta x}\ \chi_{[x_k,x_{k+1}]}(x_*) \qquad (A18)$$

is periodic and piecewise linear with equilibria still at the mid points $x_k + \Delta x/2$, see figure 16 and at the lattice points has the same value $2\pi q$ as for a point particle . Here the field of all the particles is

$$E_k = \langle E_k\rangle + p\sigma_{E_k} = 2\pi q\left(2k\,\frac{N}{K} + p\Big(1 - \frac{4k^2}{K^2}\Big)^{1/2}\sqrt{N}\right) \qquad (A19)$$

where $p$ is a real variable normally distributed, namely with probability density $e^{-p^2/2}/\sqrt{2\pi}$. At the origin the self force is dominated by the field fluctuations. In the nearby points $|k| = 1, 2$ the average value $N/K$ dominates the $\sqrt{N}$ fluctuation if $K < \sqrt{N}$, a condition which is satisfied by our choice $K = N^{1/3}$. Since the field grows linearly far from the origin the problem of self oscillations is not present in any case.

## References


1. I. M. Kapchinsky, V. V. Vladimirsky *Proc. 1959 Internat. Conf. High Energy Accelerators* (CERN, Geneva, 1959) 274.
2. *Theory of Resonance Linear Accelerators* (Harwood Academic Publishers, New York, 1985)
3. R. L. Gluckstern, Phys. Rev. Letters **73**, (1994) 1247.
4. R. L. Gluckstern, W. H. Cheng, H. Ye, Phys. Rev. Letters **75**, (1995) 2835.
5. R. L. Gluckstern, W. H. Cheng, S. S. Kurennoy, H. Ye, Phys. Rev E **54**, (1996) 6788.
6. H. Okamoto, M. Ikegami Phys. Rev. **55**, (1997) 4694.
7. A. Pisent, A. Bazzani, Y. Papaphilippou, M. Communian, G. Miano, V. Vaccaro, L. Verolino, G. Turchetti, Luneburg 1977, DESY Proceedings **1998-03**, (1998), 195.
8. A. Bazzani, M. Communian, A. Pisent, Part. Accel. **63** (1999), 79.
9. M. Lagniel, Necl. Instr. Meth. A **345**, (1994) 405.
10. F. Bergamini *Non linear effects in high intensity beams* (Phys. Dep. of Bologna University thesis 2000) unpublished.

11. G. Turchetti, A. Bazzani, F. Bergamini, S. Rambaldi, I. Hofmann, L. Bongini, G. Francheti, NIM **464**, (2001) 551.
12. K. C. Birsdall and A. B. Langdon, *Plasma physics via computer simulation* (Mc Graw Hill, New-York 1985)
13. A. Friedman, D.P. Grote, and I. Haber, Phys. Fluids **B 4**, (1992) 2203.
14. R. L. Gluckstern, A. V. Fedotov, S. Kurennoy, R, Ryne Phys. Rev. **58**, 4977 (1998).
15. D. Neuffer, IEEE Trans. Nucl. Sci. **NS 26**, (1979) 3031.
16. M. Communian, A. Pisent, A. Bazzani, G. Turchetti, S. Rambaldi, Physical Review Special Topics - Accelerators and Beams **4**, 124201 (2001).
17. M. Reiser, *Theory and design of Charged particles beams* (J. Wiley and Sons, New York, 1994)
18. R. L. Gluckstern, (Proceedings of the Linac Conference, Fermilab, Batavia, 1970) 811.
19. I. Hofmann, Phys. Rev. E **57** (1998) 4713.
20. J. Struckmeier, Phys. Rev. **E 54**, 830 (1996).
21. R. Davidson, Phys. Rev. Letters **81**, (1998) 991.
22. http://trasco.lnl.infn.it
23. R. W. Hockney and J. W. Eastwood, *Computer Simulation Using Particles*, (Adam-Hilger, Bristol, 1988)
24. A. Franchi, S. Rambaldi, G. Turchetti *HALODYN: documentation and users manual* available from franchi@gsi.de
25. G. Franchetti, I. Hofmann, G. Turchetti (Luneburg 1997,DESY Proceedings 1998-03, 1988) 183.
26. F. Bergamini, G. Franchetti, G. Turchetti, Il Nuovo Cimento A **112**, (1999) 429.
27. G. Kellog, *Foundations of potential theory* (Dover Publications, New York, 1953)
28. C. Agostinelli, *Istituzioni di Fisica Matematica* (Zanichelli, Bologna, 1960)
29. Bartolini, , A. Bazzani, M. Giovannozzi, W. Scandale, E. Todesco, Part. Accel. **52** (1996) 147, **55**, (1996) 247.
30. J. Laskar, Physica D **67**, (1993) 257.
31. C. R. Prior, *Simulation with space charge* Workshop in Space Charge Physics in High Intensity Hadron Rings, New York, 1998, (Ed A. U. Luccio, W. T. Weng AIP AIP Proceedings **448**, 1998) 85
32. A. Friedman, D. P. Grote, D. A. Callaham, A. B. Langdon, I. Haber. Particle Accelerators **37**, (1992) 131.
33. A. Franchi private communication.